RESEARCH ARTICLES

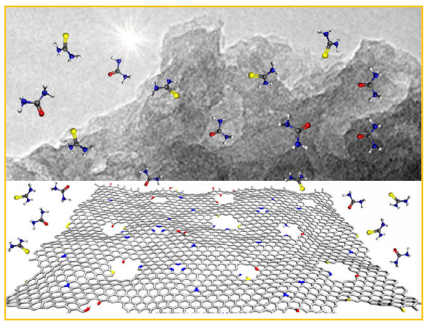

Ball-milling (BM) method is used for nitrogen and sulfur-doping graphene oxide (GO). Urea or thiourea are mixed and subjected to a solid-state grinding process. The elemental composition of BM-GO-urea exhibits 7.7 at% of nitrogen, whereas BM-GO-thiourea displays 6 at% of sulfur with 5.6 at% of nitrogen. Urea and thiourea interacting with graphene-sheets are investigated by density functional theory (DFT) calculations.

ADVANCED ENGINEERING MATERIALS
www.aem-journal.com

Nitrogen and Sulfur Incorporation into Graphene Oxide by Mechanical Process

Roque Sánchez-Salas, Emilio Muñoz-Sandoval, Morinobu Endo, Aarón Morelos-Gómez, and Florentino López-Urías*

Graphene oxide (GO) is one of the carbon nanomaterials used most in novel applications. Due to its easy synthesis, easy exfoliation, doping potential performance, and good compatibility in composites, GO has attracted the attention of several research groups. The introduction of foreign atoms into this nanomaterial can enhance its chemical and physical properties. The milling method is used for reducing and doping of GO during the mechanochemical process, using urea and thiourea as dopant agents and solid grinding molecule assistant. The elemental composition of BM-GO-urea exhibits 7.7 at% of N, whereas BM-GO-thiourea displays 6 at% of S with 5.6 at% of N. Using density functional calculations, urea, and thiourea molecules are covalently joined to the carboxyl-functional groups. After structure optimization, the density of states, highest occupied molecular orbital (HOMO), and lowest unoccupied molecular orbital (LUMO) wave functions are analyzed. It is shown that nitrogen doping favors a HOMO energy decrement when the molecules are directly attached to graphene sheets in the absence of carboxyl groups, making it energetically less expensive to share electrons in undoped nanomaterials. In contrast, the urea and thiourea molecules joined to graphene sheets via carboxyl groups show deep HOMO energies and low nitrogen-doping variations. Our results demonstrate the viability of the high-energy ball milling (HEBM) technique for reduction and N/S doping-functionalization of GO and a mechanochemical methodology to exfoliate and dope-functionalize graphite.

1. Introduction

The physical and chemical properties of graphene oxide (GO) have been widely studied.[1–3] One important characteristic of GO, after its fabrication, is its covalent or noncovalent functionalization. As GO shows good biocompatibility, it has been used as a drug-delivery system.[4] For environmental remediation, the oxygen functional groups of GO help to remove heavy metals in the liquid media.[5,6] Further, GO has been decorated with nanoparticles as hybrid materials for catalyst performance.[7] For water treatment, GO has been used as a membrane, exploiting its antifouling properties, facile, and large-scale production.[8] GO has been proposed as an ideal candidate for nanomedicine applications and a biomolecule nanocarrier.[9]

Recently, the incorporation of foreign atoms or molecules on GO has been suggested as an anode for lithium-ion batteries.[10] Nitrogen and phosphorus dual-doped reduced GO has been synthesized by heating GO, urea, and 1,2-bis (diphenylphosphino) methane. Their lithium-ion storage performance was tested, resulting in a better material for the charge and discharge process. Urea and thiourea are excellent candidates for incorporating nitrogen into graphitic materials via the milling method, using GO or graphite materials. Both urea and thiourea are water-soluble and environmentally-friendly, with a mild chemical reduction activity on GO via deoxygenation of the two amine $-NH_2$ groups at the oxygen functional groups. Earlier investigations reported covalent cross-linking when thiourea and urea are included between the GO sheets due to the weak interlamellar interaction and stacked 2D channels with potential molecule selectivity on aqueous GO dissolutions and paper-like membrane.[11,12]

Other groups investigated mixing solid N-containing organic molecules in the graphite grinding process as a simultaneous N doping and solid grinding agent during the milling process, known as solid-state dope/functionalized graphitic sheets, via dry milling with a post-purification step, as the molecule was water-soluble. Xue et al.[13] used melamine ($C_3H_6N_6$) and graphite in a 10:1 mass proportion to obtain by milling N-doped graphene nanoplatelets with a C/N ratio of 7.4 and evidence

R. Sánchez-Salas, E. Muñoz-Sandoval, F. López-Urías
División de Materiales Avanzados
IPICYT
Camino a la Presa San José 2055, Lomas 4a sección, San Luis Potosí 78216, México
E-mail: flo@ipicyt.edu.mx

R. Sánchez-Salas, M. Endo, A. Morelos-Gómez
Research Initiative for Supra-Materials
Shinshu University
4-17-1 Wakasato, Nagano 380-8553, Japan

M. Endo, A. Morelos-Gómez
Global Aqua Innovation Center and Research Initiative for Supra-Materials
Shinshu University
4-17-1 Wakasato, Nagano 380-8553, Japan

The ORCID identification number(s) for the author(s) of this article can be found under https://doi.org/10.1002/adem.202001444.

DOI: 10.1002/adem.202001444

of N-pyridinic, N-quaternary, and N-pyrrolic doping. Further, Liu and co-workers[14] used solid urea (CH_4N_2O) and graphite in a 20:1 mass proportion in the milling process, to obtain nitrogen-doped graphene nanosheets with a C/N ratio of 28.7, also with evidence of nitrogen doping into the hexagonal plane with a majority part of N-pyrrolic.

In this work, an inexpensive process has been implemented to fabricate GO with attached nitrogen and sulfur-containing molecules at the surface. By a simple mixing of GO with urea and thiourea using a ball-milling (BM) process, we obtained a novel nanomaterial with interesting chemical and physical properties.

2. Results and Discussion

The morphology of the samples after BM was observed by scanning electron microscopy (SEM); **Figure 1**a–c shows the SEM images of GO-BM, GO-T-BM, and GO-U-BM samples. Sample GO-BM exhibited grain size with diameters ranging from 10 to 960 μm^2 (Figure S4a, Supporting Information), GO-T-BM showed grain sizes of 5–46 μm^2 (Figure S4b, Supporting Information), and GO-U-BM grain sizes of 1–172 μm^2 (Figure S4c, Supporting Information), with an average of 119, 16, and 26 μm^2, respectively. SEM images for G-BM, G-T-BM, and G-U-BM are shown in Figure 1d,f with respective average

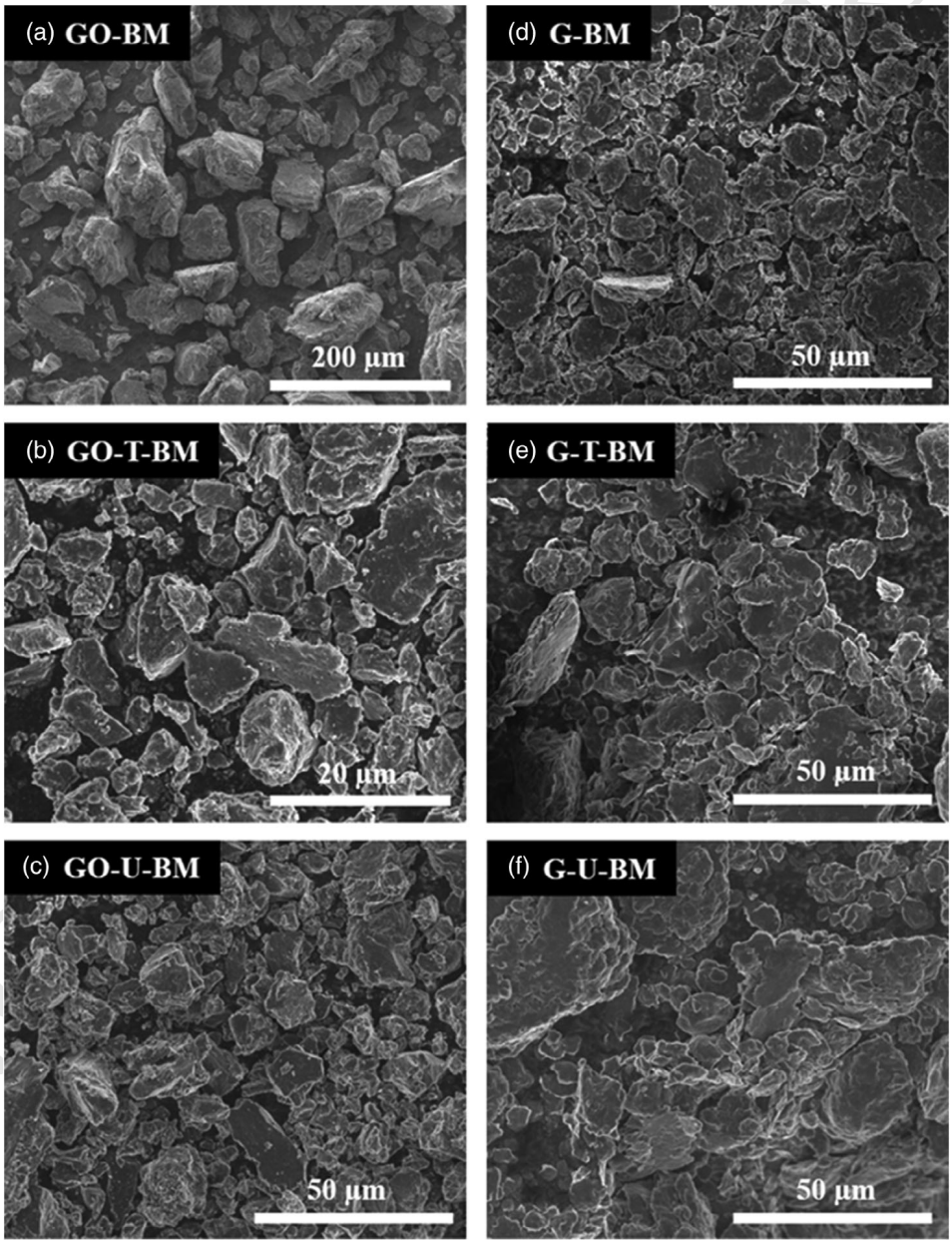

Figure 1. SEM images of a) GO-BM, b) GO-T-BM, c) GO-U-BM, d) G-BM, e) G-T-BM, and f) G-U-BM. The grain size distribution can be seen in Figure S4, Supporting Information. All samples exhibited a polydispersity in grain size and morphology. The GO-T-BM showed the smallest grain size area down to 5 μm^2 in diameter. Notice that the use of urea and thiourea influence the grain size and morphology of the grains.

sizes of 22, 23, and 24 μm^2, with similar size, ranging between 1 and 150 μm^2. Energy-dispersive X-ray spectroscopy (EDS) of the samples is shown in Figure S5, Supporting Information, with their respective atomic concentration. As expected, the GO-based samples showed the highest oxygen contents concerning graphite-based samples; see Figure S5a–c, Supporting Information. The use of urea provided the highest nitrogen concentrations for samples GO-U-BM and G-U-BM (Figures S5c and S5f, Supporting Information). In contrast, with thiourea, the highest sulfur content was found for the sample GO-T-BM, followed by sample G-T-BM (Figures S5b and S5e, Supporting Information). The sulfur traces in sample GO-BM and GO-U-BM come from the GO preparation (Figures S5a,c, Supporting Information). **Figure 2** shows the transmission electron microscopy (TEM) and HRTEM images of GO. The structural damages are notable in the TEM images of GO-based materials. Holey-like structures were observed in GO-T-BM and G-T-BM samples, due most likely to the mechanochemical decomposition of thiourea into graphitic carbon nitride nanocomposites between 500 and –600 °C under air or inert atmosphere;[15–19] moreover, hole damages were observed in graphite milled sample with thiourea (Figure S7–S8, Supporting Information).

The BM process for graphitic-based materials (G-BM, G-T-BM, and G-U-BM) causes other structural damage compared to GO, due to the higher mechanical properties of the graphite layers, as shown in **Figure 3**, exhibiting usual top-to-down graphite exfoliation with few-layered sheet nanostructures and well-graphitized stacked-layer planes with similar layered distance stacking. Figure S6, Supporting Information, shows HRTEM images and interatomic distance profiles of the (002) crystallographic plane.

The sample's crystal structure was characterized by X-ray diffraction (XRD). **Figure 4**a–d shows the XRD patterns for milled GO-based samples. The graphitic (002) peak for GO-BM, GO-T-BM, GO-U-BM was found at $2\theta = 24.7 \pm 0.46°$, with an interlayer distance of 3.59, 3.58, and 3.49 Å, respectively. The GO (001) area peaks were 9.6%, 14.8%, and 31.6%, compared to their respective graphitic (002) peak. We identified the

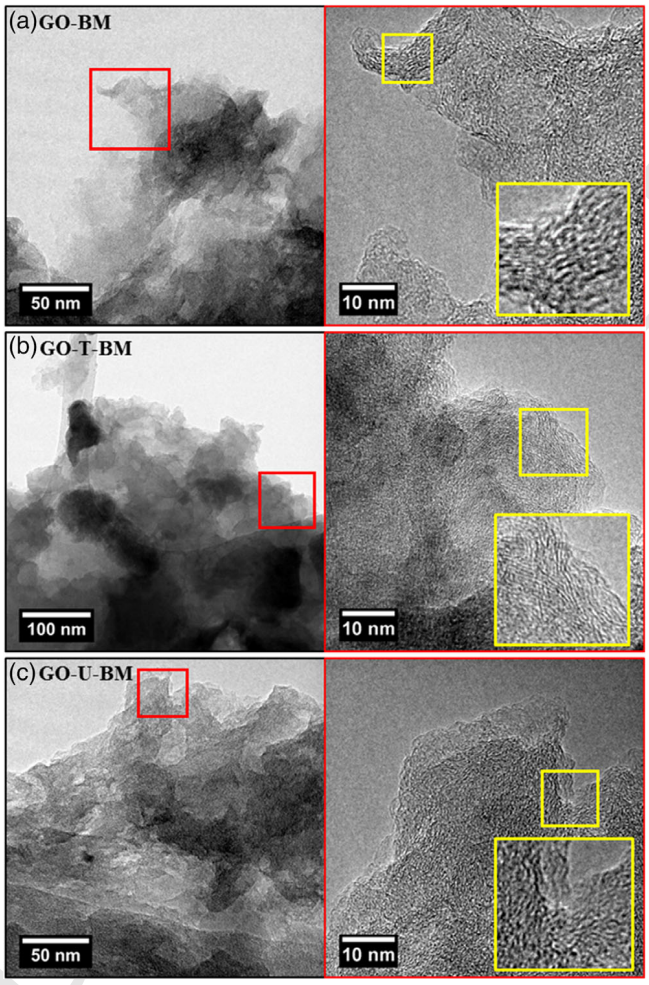

Figure 2. TEM and HRTEM images of a) GO-BM, b) GO-T-BM, and c) GO-U-BM. The corresponding enclosed areas in red color are shown on the right side. All samples exhibited corrugated reduced GO sheets with irregular edges. Complementary TEM images for GO milled samples can be seen in Figure S7, Supporting Information.

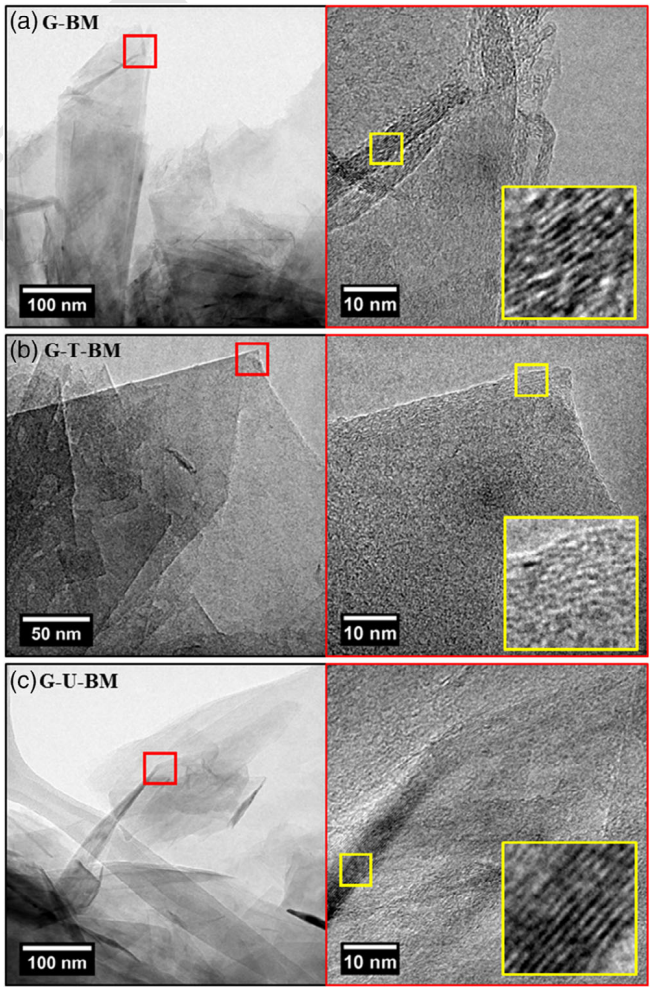

Figure 3. TEM and HRTEM images of a) G-BM, b) G-T-BM, and c) G-U-BM. In (a–c) the graphitic structures exhibits few layered graphenic sheets. The square yellow insets show stacked graphitic layers. Complementary TEM images for graphite-milled samples can be seen in Figure S8, Supporting Information.

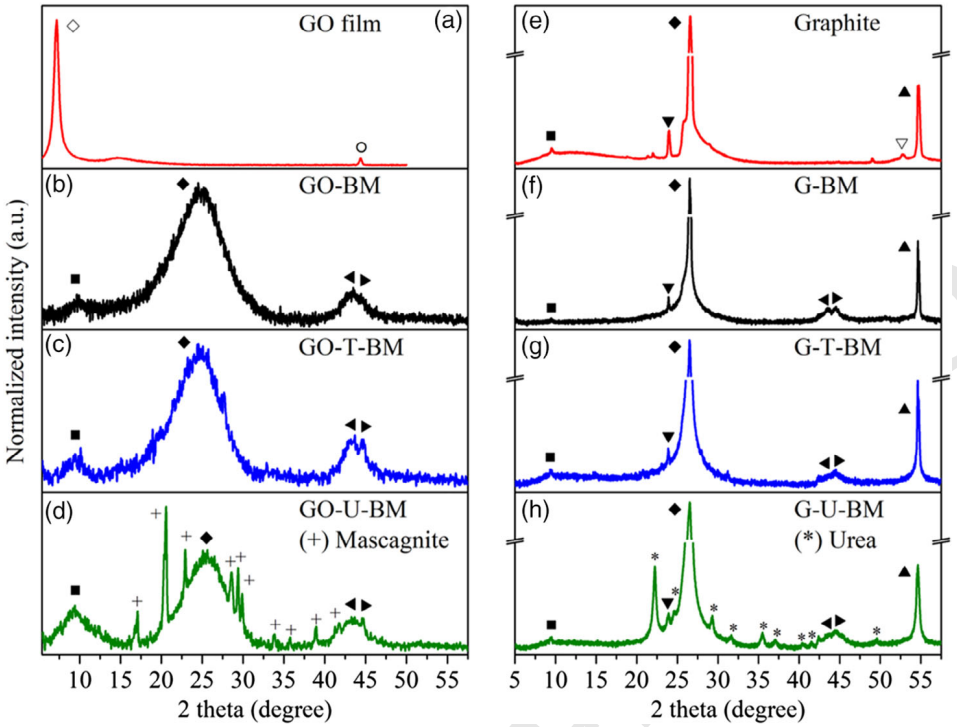

Figure 4. XRD patterns for a–d) GO materials and e–h) graphite materials. The symbols refer to different crystallographic planes: left triangle (001), square and empty rhomb (001), full rhomb (002), down triangle K_β(002), left triangle (001), right triangle (101), up triangle (004), and empty down triangle K_β(004). For (f–h), the crystalline sizes $Lc_{(002)}$ were 34, 32, and 15 nm, respectively. Additionally, ammonium sulfate (Mascagnite) peaks (ICDD #40-0660) and urea peaks (ICDD #08-0822) were found in GO-U-BM and G-U-BM samples with a residual percentage of 7.3% and 8.6%, respectively.

ammonium sulfate $(NH_4)_2SO_4$ diffraction peaks in GO-U-BM, called Mascagnite, suggesting that amino groups might be reduced to ammonium (NH^{4+}) and be made salts with sulfate ions ($SO4^{2-}$) from residual GO synthesis during the milling process. XRD results for milled graphite-based samples are shown in Figure 4f–h, revealing the (002) diffraction peak at $2\theta = 26.51° \pm 0.02$ with an interlayer distance of 3.36 Å but full width at half maximum (FWHM) of 0.20, 0.25, and 0.43 for G-BM, G-T-BM, and G-U-BM, respectively. For GO-U-BM, the additional diffraction peaks coincide with those of urea. This fact could be due to the higher energy decomposition of the urea molecule. The average crystallite size for the graphite-based BM samples was estimated using the Scherrer's Equation $D(hkl) = K\lambda/\beta\cos\theta$ at the (002) graphitic peak, where K is a constant taken as 0.89, λ is the X-ray wavelength (nm), and β is the FWHM of the considered diffraction peak. Then, crystalline sizes were 34, 32, and 15 nm for G-BM, G-T-BM, and G-U-BM, respectively, which confirmed that urea remains to act as a solid grinding agent. Raman spectrum was adopted to study the graphitic nature of the samples; the D, G, G′, D + D″, 2D, and D + D′ bands for GO-based and graphitic-based samples are shown in **Figure 5**a,c. Furthermore, the pristine reference was added. It is noteworthy that all the GO-based samples showed less than one I_D/I_G ratio (see Figure 5b). The corresponding Raman shift band positions and FWHM dispersions are shown in Figure 5b, d. In GO-based materials, GO-T-BM showed the lowest graphitization ratio I_D/I_G, lowest FWHM of D and G bands, and shorter down-Raman shift for G and 2D bands, compared to GO-BM. These findings suggest a higher density from concurring defects as an indicator of an N, N–S doping, or functionalized edges due to thiourea. In addition, GO-BM had the highest graphitization quality ratio I_D/I_G. The highest FWHM for the D and G bands from milled GO-based samples could indicate different border disorders or defect differences at graphitic defects and active sites.

Alternatively, milled graphite-based samples showed an increment in their D band due to the structural exfoliation damage (Figure 5c). Top-to-down exfoliated graphite displays an increase in the D′ band at ≈1620 cm^{-1} (just next to G-band), usually indicating the presence of edge defects in the graphitic lattice,[20] as well as an N doping contribution in the G-T-BM and G-U-BM cases.[21] Therefore, the I_D/I_D ratio could be used as a parameter of defects at the borders in the exfoliated graphitic material related to sp^3-like vibration modes.[22,23] The G-T-BM sample presents the lowest graphitization ratio I_D/I_G, lower FWHM of the D and G bands, with a down-Raman shift position of the G and 2D bands, compared to the G-BM sample. Finally, $I_D/I_{D'}$ ratio shows the highest value in Figure 5d for G-T-BM and matched in the conjecture of higher density from concurring defects or incorporation of N, N-S doping borders concerning G-U-BM. However, after the milling process, the FWHM for the D band had the highest value for G-BM, followed by G-T-BM and the lowest for G-U-BM as an indication of higher to smaller active sizes, respectively.

The thermal decomposition of the samples was studied by thermal gravimetry analysis (TGA). **Figure 6** shows the TGA

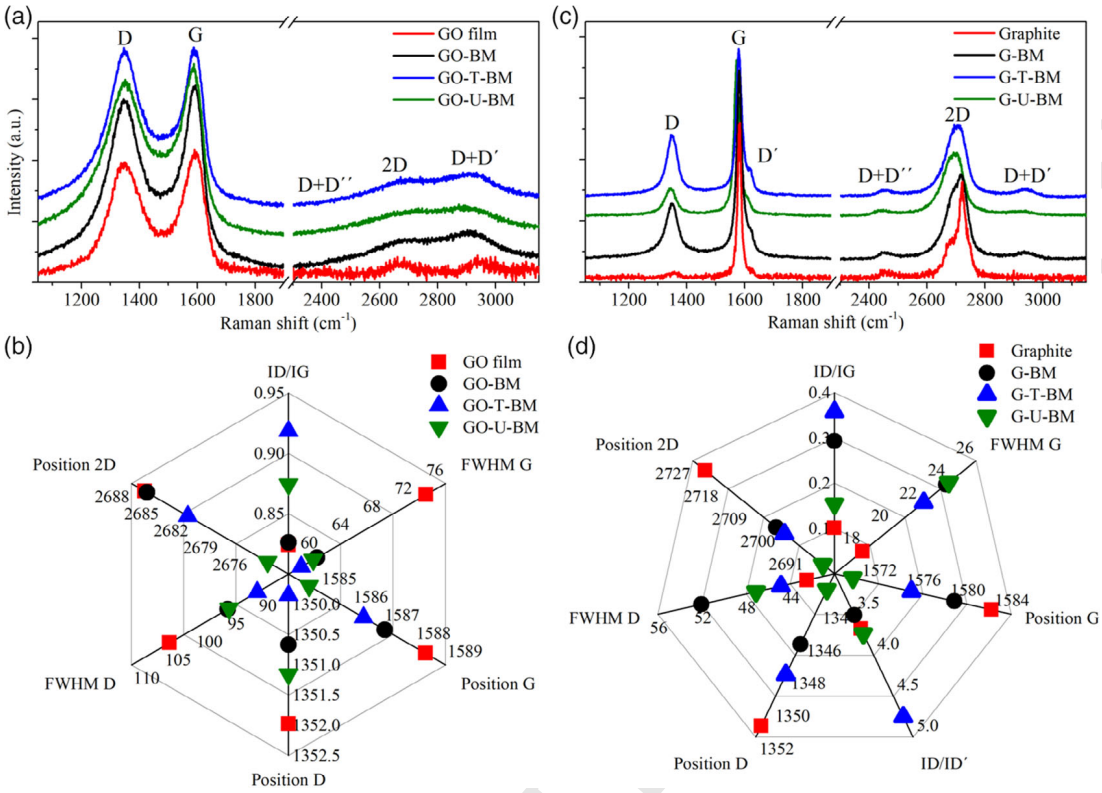

Figure 5. Raman spectra for a) GO and c) graphite materials (pristine and BM). b,d) Radar plots showing the ratio of intensities between the D- and G-bands (I_D/I_G) with their FWHM and peak position of D, G, and 2D bands for GO and graphite samples, respectively. $I_D/I_{D'}$ ratios were estimated from graphitic-based samples. Values shown in (b) and (d) can be seen in **Table 1**.

curves for milled graphite-based and GO-based samples. The onset point for GO-BM, GO-T-BM, and GO-U-BM samples was found at 484, 533, and 552 °C, respectively (Figure 6a) with weight losses over four intervals: 1) 50–130 °C due to the water evaporation on the surface and inter/intralayer due to their hygroscopic nature derived from the oxygen functionalities, 2) 130–220 °C corresponds to the residual decomposition of oxygenated functional groups (carbonyl and carboxyl), 3) 220–420 °C due to the decomposition in more complex oxygenated functional groups (lactone-ester, carboxylic-anhydride, phenol, ether, carbonyl),[24] 4) 420–650 °C, which is assigned to the decomposition of turbostratic reduced-GO and finally graphitic decomposition after 650 °C.[25–27] The thermogram exhibits water desorption below 160 °C, with a weight loss of 18% regarding the GO-film. Then, between 160–226 °C, we found an onset point at 206 °C. The sample underwent an accumulative weight loss of 29% due to the decomposition of oxygenated groups, then a gradual decomposition of more stable oxygenated functional groups of ≈4 wt% every 100 °C up to 600 °C, and finally, the graphitic decomposition ≈9 wt% every100 °C up to 950 °C. Finally, due to the premixture of the urea and thiourea with the GO, their mild chemical reduction potential enhanced the thermal oxidation stability compared to GO pristine milling. On the other hand, we found that milled graphite-based samples exhibited a weight loss of less than 1 wt% before 160 °C. The samples G-BM, G-T-BM, and G-U-BM showed an onset temperature of 544, 592, and 614 °C (Figure 6b), respectively. It was noticed that under 350 °C, the TGA curves were different due to the raw thiourea/urea residue. For instance, the mass losses of G-T-BM matched with the thiourea molecule at 180, 220, and 250 °C.[28,29] Furthermore, sample G-U-BM exhibited two mass losses at 200 and 320 °C attributed to the urea molecule.[30] To conclude, the BM decreases the thermal oxidation stability of graphite. Interestingly, urea and thiourea exhibit higher stability than without these dopant/reducing precursors from the TGA observations; urea and thiourea aid to increase the chemical stability of GO with BM.

We now discuss the XPS characterizations to study the surface chemistry. **Figure 7** shows the atomic percent derived from the XPS survey spectra (see also Figure S9, Supporting Information). **Figure 8** shows the high-resolution XPS for pristine and milled GO-based samples. The C1*s* spectra for GO-BM showed remarkable changes, compared to the as-produced GO (Figure 8a). The milled GO-based samples exhibited an attenuated peak around 286.7 eV related to C—O and C═O bonds (epoxy, carbonyl, and carboxyl groups). This indicates a partial reduction process of GO by mechanochemical processes, combined with urea and thiourea, were observed in peaks attributed to C═C and C—C bond (sp^2 and sp^3 carbon hybridization). The GO-film showed a broader peak due to the high concentration of sp^3 hybridization, and the BM samples exhibited narrow graphitic peaks. The C═O/C—C peak for GO-BM showed a peak centered C═C energy. Those milled with urea or thiourea exhibited a binding energy shift toward the C—C bond, larger for the GO-U-BM

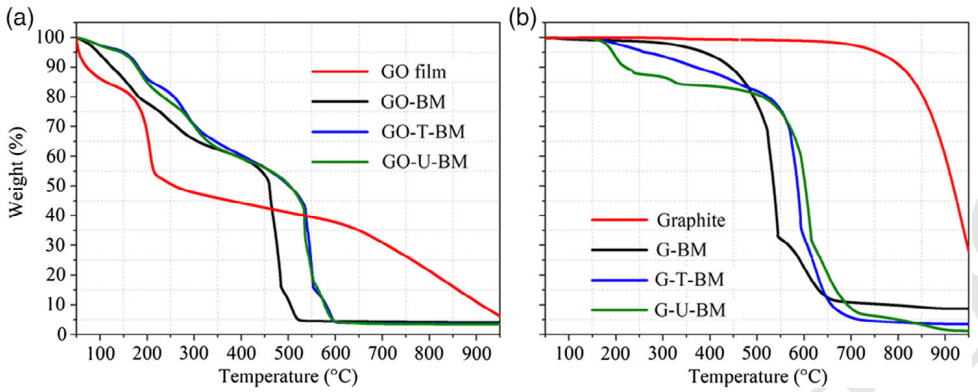

Figure 6. TGA curves for a) pristine GO and BM GO materials. The onset temperature for GO-BM, GO-T-BM, and GO-U-BM samples are located at 484, 533, and 552 °C, respectively. The GO pristine exhibited a significant loss of weight (≈25%) at ≈200 °C. b) TGA curves for pristine graphite and BM graphite materials; the onset temperatures are 544, 592, and 614 °C for G-BM, G-T-BM, and G-U-BM, respectively. The pristine graphite exhibited an onset temperature of ≈935 °C.

Table 1. Raman characterization data from radar plots (see Figure 5).

Sample	Band	FWHM	Position	$I_D/I_{D'}$ ratio	I_D/I_G ratio
GO film	D	103.9 ± 17.1	1351.9 ± 0.1		0.82 ± 0.03
	G	73.5 ± 8.1	1588.3 ± 1.5		
	2D	170.5 ± 11.7	2686.6 ± 3.8		
GO-BM	D	94.6 ± 0.9	1350.6 ± 0.8		0.83 ± 0.03
	G	59.6 ± 0.9	1587.0 ± 0.5		
	2D	227.8 ± 20.8	2686.4 ± 4.5		
GO-T-BM	D	89.9 ± 1.0	1349.8 ± 0.8		0.93 ± 0.02
	G	57.6 ± 0.7	1586.3 ± 1.6		
	2D	218.5 ± 2.8	2682.2 ± 6.9		
GO-U-BM	D	94.4 ± 7.4	1351.1 ± 1.0		0.87 ± 0.10
	G	59.1 ± 2.8	1584.6 ± 4.1		
	2D	227.1 ± 14.9	2674.1 ± 4.5		
Graphite	D	42.5 ± 0.0	1351.3 ± 0.5	3.7 ± 0.1	0.10 ± 0.04
	G	17.9 ± 1.3	1582.2 ± 0.3		
	2D	38.5 ± 2.2	2723.0 ± 1.7		
G-BM	D	52.0 ± 4.1	1346.3 ± 2.9	3.5 ± 0.5	0.29 ± 0.02
	G	23.8 ± 4.3	1578.8 ± 4.7		
	2D	89.5 ± 7.2	2700.4 ± 4.6		
G-T-BM	D	44.8 ± 0.8	1348.1 ± 1.5	4.7 ± 0.4	0.36 ± 0.07
	G	22.3 ± 0.1	1574.9 ± 2.4		
	2D	85.8 ± 0.9	2697.8 ± 2.9		
G-U-BM	D	47.0 ± 0.3	1342.9 ± 0.5	3.7 ± 0.1	0.15 ± 0.02
	G	24.0 ± 4.6	1569.6 ± 3.6		
	2D	83.6 ± 0.1	2685.6 ± 6.2		

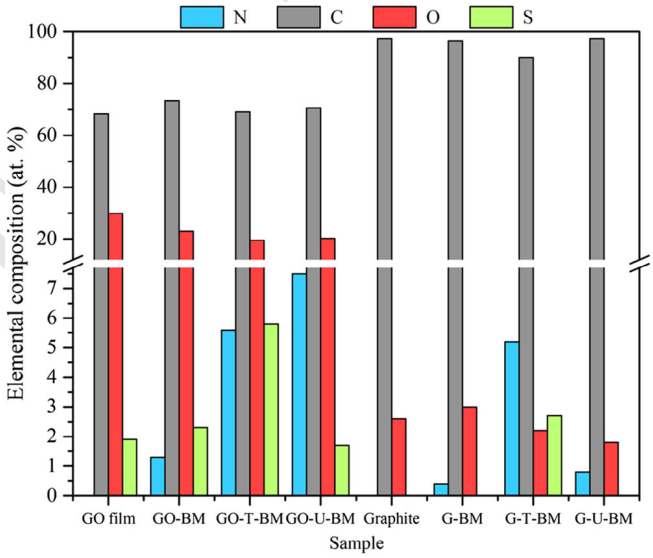

Figure 7. Estimated atomic percent concentration for elemental composition (at%) derived from the XPS survey spectra. In gray (carbon), red (oxygen), green (sulfur), and blue (nitrogen). The XPS survey spectra can be seen in Figure S9, Supporting Information.

sample. This binding energy shift could result from urea and thiourea or chemical species derived therefrom being anchored to the surface or edges of graphite sheets. Many aspects and trends of the C1*s* spectra can be supported by the O1*s* spectra (Figure 8b). The GO-film displayed an O1*s* peak centered at 532.4 eV attributed to C—O bonds due to carboxyl and epoxy groups with two more peak contributions of —OH (hydroxyl groups) at 533.3 eV and C=O (carbonyl, carboxyl, amide groups) at 531.1 eV. The GO-milled samples showed O1*s* peak asymmetry broadness. The irregular width shape observed in milled GO samples could be due to a wide variety of oxygen, nitrogen, or sulfur functional groups attached to the edges, probably due to amides ($C—NH_2$), ammonia ($C—NH3^+$), nitrogen oxide (NOx), and sulfur oxide (SOx). For N1*s* spectra (Figure 8c), the GO-film did not exhibit a nitrogen signal (red line); however, the GO-BM sample yielded a signal centered at the N-pyrrolic position (**Figure 9**c). GO-U-BM showed an N1*s* peak centered at the N-pyrrolic position with significant NOx traces. Similar behavior was observed for GO-T-BM, where the maximal peak intensity corresponded to N-pyrrolic and, subsequently, to quaternary nitrogen (NQ). $C—NH_2$ could be found at ≈399.5 eV and

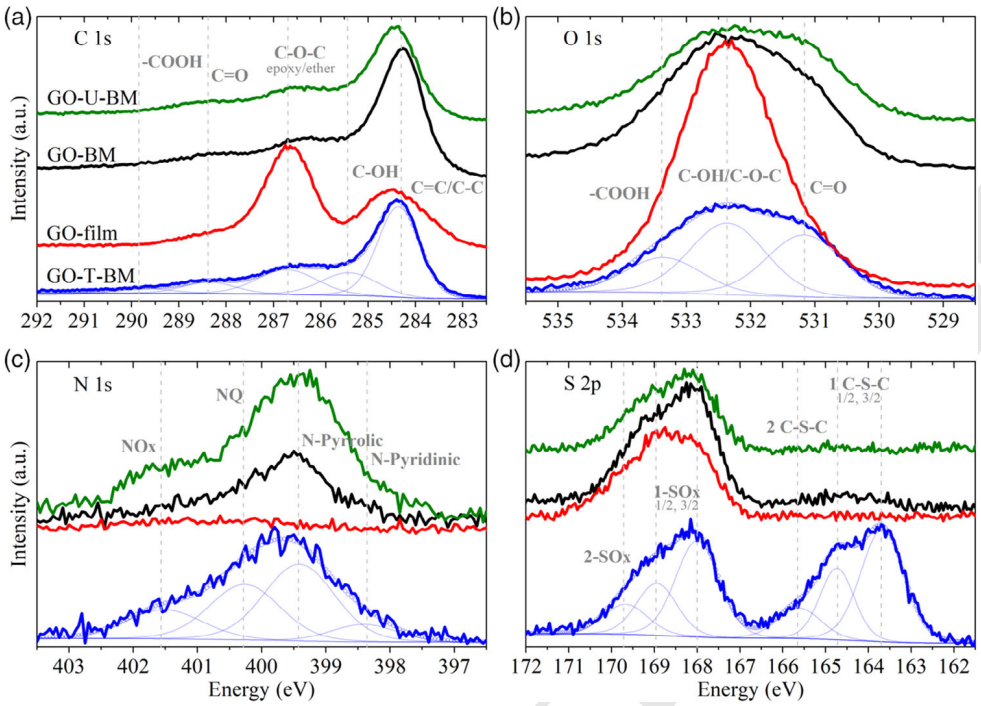

Figure 8. High-resolution XPS spectra for pristine GO-films and BM-GO materials, with thiourea (GO-T-B) and urea (GO-U-BM). Results for a) C1*s*, b) O1*s*, c) N1*s*, and d) S2*p*. The pristine GO film (red lines) exhibited the typical C1*s* and O1*s* peaks suggesting the presence of hydroxyls (C—OH), carbonyl (C═O bonds), and carboxyl groups (C═O and C—O bonds), and likely epoxy groups (C—O—C bonds). For all samples, we identified the sulfur oxide (SOx) in S2*p* spectra; here, the sulfur comes from the GO fabrication.

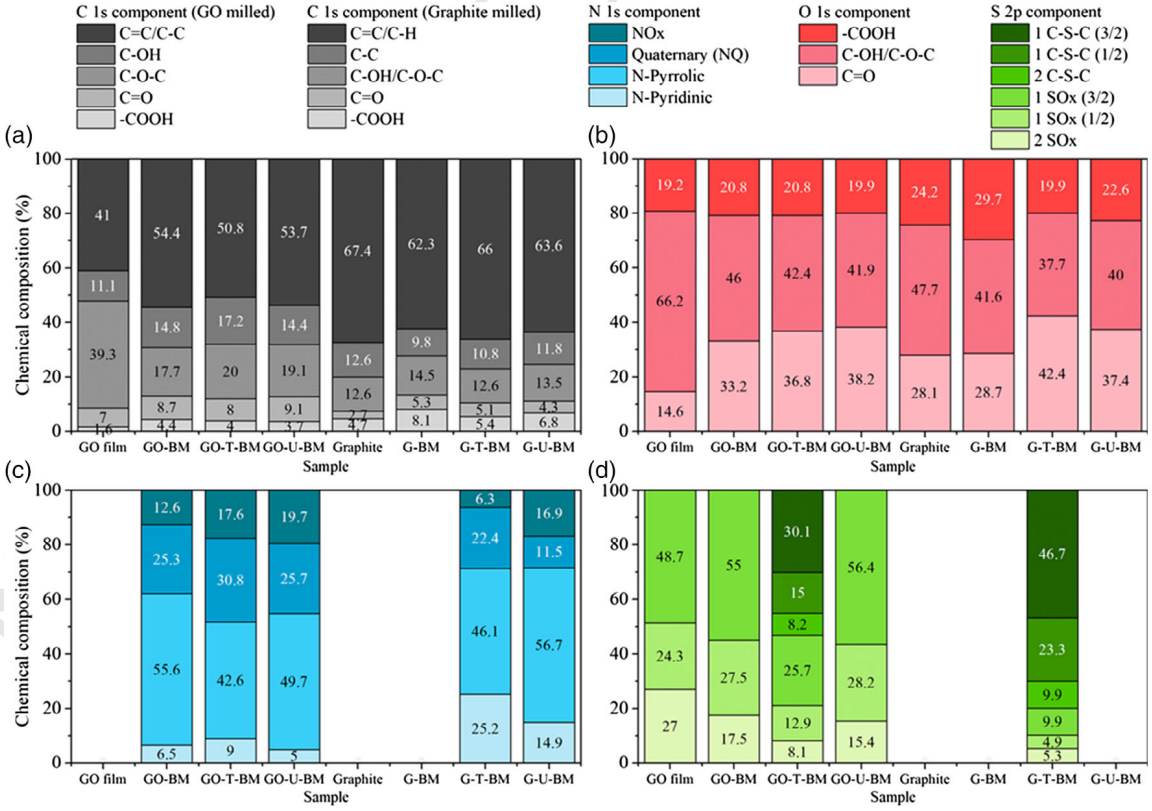

Figure 9. Estimation of the different chemical species derived from the deconvolution analysis of high-resolution XPS spectra (the percentage is indicated). Chemical species containing a) carbon, b) oxygen, c) nitrogen, and d) sulfur.

C—NH_3^+ at ≈401.6 eV.[31] The S2*p* spectra showed two signal distributions, one of them related to a group of oxidized sulfur groups signals (—SOx—) ≈168–170 eV, which were found for all samples, suggesting its origin from the GO synthesis process. The second group at binding energies ≈164 eV was found for GO-T-BM, attributed to sulfur bride species C—S—C bonds.

Figure 10 shows the high-resolution XPS for milled graphite-based samples. The narrow C1*s* peaks centered at ≈284.4 eV associated with the C═C bonds reveal the dominance of sp^2 hybridizations (Figure 10a). The low concentration of sp^3 bonded carbons (C—C) indicates nonsubstantial structure damages. O1*s* spectra (Figure 10b) of graphite showed a high binding energy shift toward —OH and C—O functionalities. The O1*s* peak (sample G-T-BM) is more centered at the C—O and C═O bonds. These samples should not have oxygen (G-BM, G-T-BM, and graphite). However, it could be due to the unavoidable oxygen from the environment reacting with the carbon-dangling bonds produced during BM or physisorbed. Figure 10c shows the N1*s* spectrum with remarkable peaks for G-U-BM and G-T-BM samples. These peaks were centered at N-pyrrolic binding energies with an essential NQ and N-pyridinic contribution, as the deconvolution analysis showed. We observed significant signals associated with SO_x and C-S-C chemical species, only for sample G-T-BM (Figure 10d).

The electrochemical characterizations were evaluated by the cyclic voltammetry (CV) technique. **Figure 11**a shows the GO-film *I*–*V* curve, and a ≈10 kΩ Ohmic resistance signature by the two-probes method was obtained.[32] We estimated the specific capacitance from the charge and discharge model $Cp = A/2mk(V2 - V1)$ from the CV curve, where *A* is the area enclosed by the CV loop, *m* the mass of material at the working electrode, *k* the scan rate, and (V2 − V1) is the potential window. Table S1, Supporting Information, shows the estimated specific capacitance of all the milled samples. Figure 11b shows the electrochemical response of the milled GO samples; the GO-BM sample showed the largest specific capacitance due to the higher density of active sites in concordance with their TGA results. Interestingly, the specific capacitance of the GO-T-BM sample was nearly 4.4 times larger than GO-U-BM, due to the difference in double-layer capacitance in the grain size area, residue of pristine GO, and water-soluble residues as mascagnite urea.

The graphite's CV plot showed a redox process corresponding to the oxidation and reduction reaction of the quinone functional group at 0.49 and 0.43 V, respectively (Figure 11c). After the mechanochemical process, considering crystallite size differences for G-BM, G-U-BM, and G-T-BM, the double-layer effect difference in the specific capacitance was between 1.9 and 2.7 times larger for G-BM, compared to G-T-BM and G-U-BM, respectively. Figure 11d is in concordance with their chemical stability temperature, graphitic crystallite size, and the graphitization quality Raman I_D/I_G ratio. We found that the milled graphite samples showed an oxidation reaction of quinone at 0.53, 0.54, and 0.51 V with their corresponding hydroquinone pair at 0.31, 0.40, and 0.38 V for G-BM, G-T-BM, and G-U-BM, respectively. Finally, G-T-BM samples exhibited electrocatalytic processes related to sulfur functionalization groups with N, O at the graphitic edges.[33–35] Based on previous reports, the G-T-BM electrocatalytic processes (blue line in Figure 11d) could be related to pyrrolic-N-sulfide, sulfhydryl oxidation (thiol) to

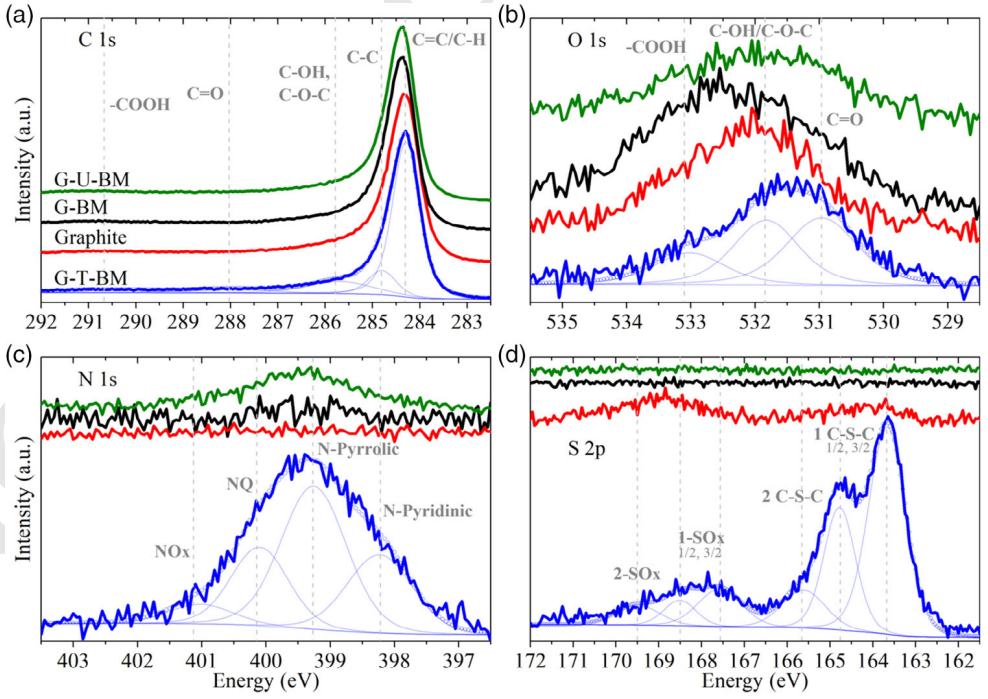

Figure 10. High-resolution XPS spectra for pristine graphite and graphite BM materials, with thiourea (G-T-BM) and urea (G-U-BM). Results for a) C1*s*, b) O1*s*, c) N1*s*, and d) S2*p*. The samples exhibited the typical C1*s* graphite materials dominated mainly by C═C bonds. Notice that the width, shape, and peak position of O1*s* spectra depended strongly on the material involved suggesting the presence of different functional groups. Notice that only G-T-BM showed S2*p* signals, suggesting the presence of C—S—C bonds.

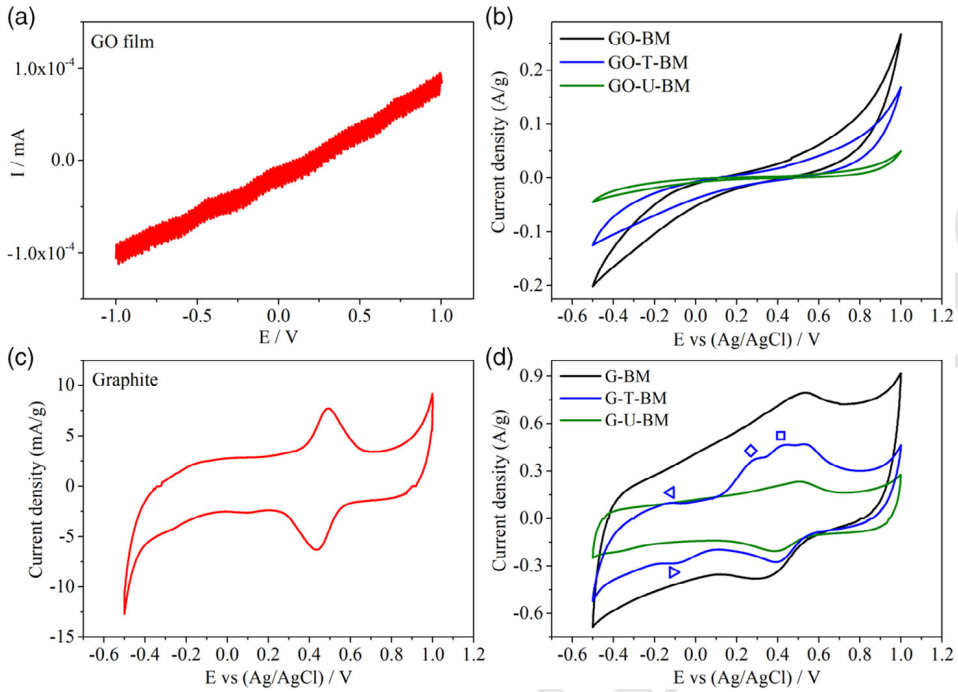

Figure 11. LSV for a) GO film, and CV measurements for b) milled GO materials with thiourea (T), urea (U), c) pristine graphite (G), and d) milled graphite materials with thiourea and urea. The GO-film exhibited almost negligible currents for this particular voltage window due to the isolator feature of GO materials.

thiolate reduction (thioketone), thiophene-like dioxide, and other oxidized sulfur —SO functional groups.[36–41]

To elucidate the role of urea and thiourea in the electronic properties of sp^2 carbon materials, we performed first-principles density functional theory (DFT) calculations on $C_{96}H_{24}$ graphene sheets with zigzag edges. We considered three different paths of anchoring urea and thiourea molecules on the graphene sheets. The molecules were anchored to the edge via the oxygen or sulfur atoms labeled as direct-urea and direct-thiourea systems, as shown in **Figure 12**a,b. The molecules were joined through their amine group and carboxylic group, using two routes for functionalized graphene sheets. For the first route, in the anchoring mechanism, the system releases two hydrogens, labeled as carboxyl–urea and carboxyl–thiourea, as in Figure 12c,d. In the second route, the systems were labeled as peptide–urea and peptide–thiourea; the anchoring was carried out via the peptide bond, as in Figure 12e,f. Here, the systems release H_2O in the anchoring process. Figure 12g shows the density of states of urea and thiourea molecules joined to the edges of the graphene sheets discussed earlier. The highest occupied molecular orbital (HOMO) and the lowest unoccupied molecular orbital (LUMO) energies showed a downshift for carboxyl-molecule and peptide-molecule systems, compared to direct-molecule systems, as in Figure 12g. **Figure 13** shows the HOMO and LUMO wave functions and their associated energies. In general, the systems showed delocalized HOMO wave functions at the entire graphene sheet and localized LUMO wave functions mainly at the urea and thiourea molecules. A significant localization of LUMO wave functions was observed in direct-urea and direct-thiourea systems (Figure 13a,b).

Now, the nitrogen-doping effects on the HOMO and LUMO energies of the structure shown earlier are discussed. Here, the nitrogen is incorporated via substitutional doping, where a carbon atom is removed and replaced by a nitrogen atom (**Figure 14**a). The nitrogen was moved from position N1 (near the anchoring sites) to N8 (away from the anchoring sites). We observed an apparent effect of nitrogen doping on the HOMO energies, mainly for direct-urea and direct-thiourea systems (Figure 14b); here, it was observed that monotonic energy decreases as the nitrogen atom moves away from the anchoring sites. These results suggest that direct-urea and direct-thiourea systems could easily donate their electrons when doped with nitrogen. Conversely, the urea and thiourea molecules attached via carboxyl to peptide bond showed lower HOMO energy with slight changes with the nitrogen doping, which should make it much more energetically expensive to remove their electrons. In electrochemical terms, the direct-urea and direct-thiourea are more susceptible to oxidization. On the other hand, we observed a low LUMO energy for carboxyl–urea, carboxyl–thiourea, peptide–urea, and peptide–thiourea systems; thus, a reduction process in these systems could be favored. We show more results for urea and thiourea molecules chemisorbed through a carboxyl group at the central part of the graphene sheets. **Figure 15** shows the optimized structures, density of states, and wave functions. In general, the systems considered exhibited electronic properties similar to HOMO wave functions localized mainly at and around the urea and thiourea molecules. In contrast, the LUMO wave function showed a delocalization on the entire body of the graphene sheets. The HOMO energies were less than those obtained for molecules joined to the ribbon's edges. Additional calculations revealed that

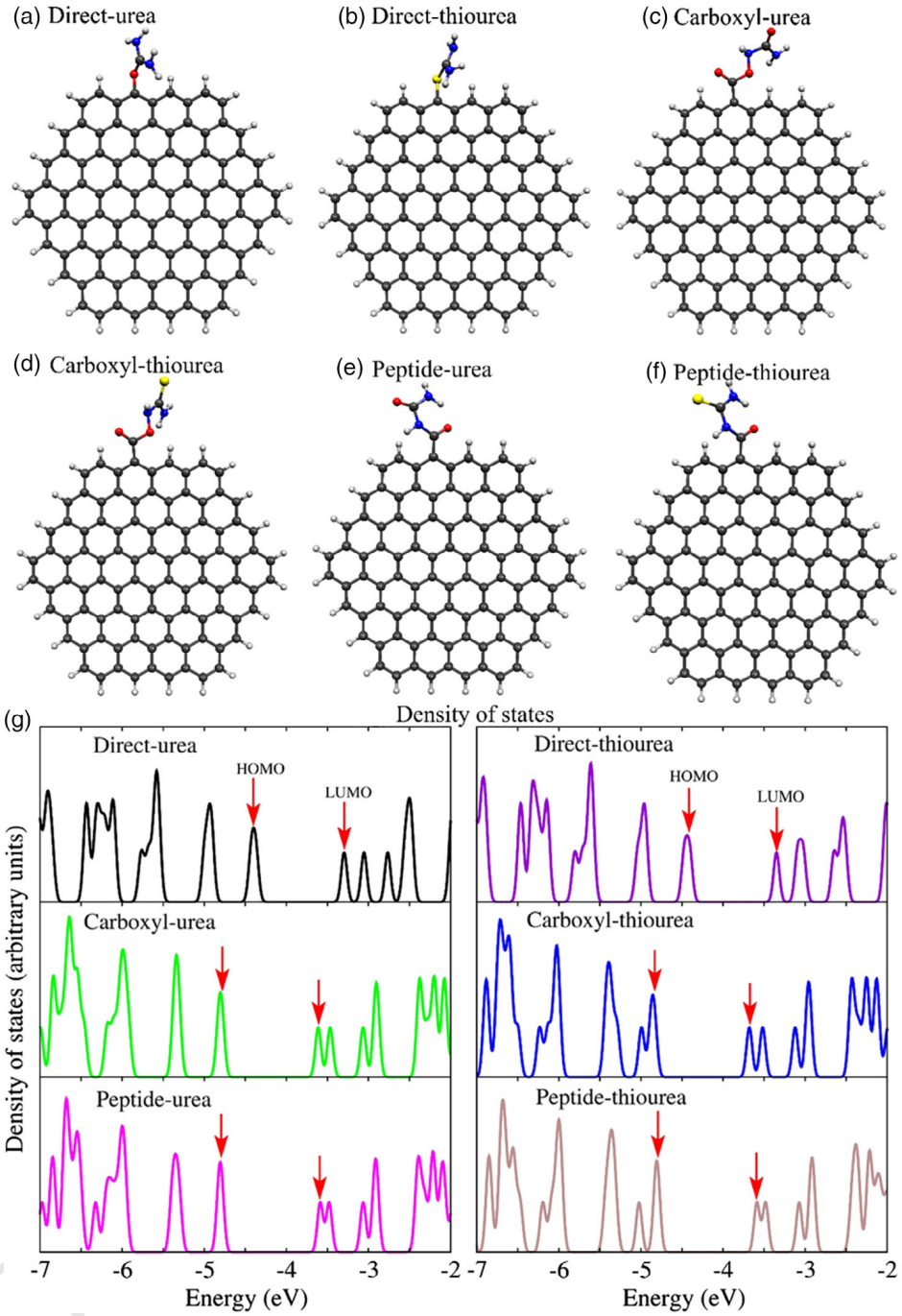

Figure 12. a–f) Ball-stick model of the optimized structures of graphene sheets $C_{96}H_{24}$ with urea and thiourea molecules covalently anchored to the edges. The hydrogen, carbon, nitrogen, oxygen, and sulfur atoms are in gray, black, blue, red, and yellow colors, respectively. g) The corresponding electronic density of states. Arrows indicate the HOMO and LUMO energies.

the molecules were not chemisorbed in pristine sheets and carbonyl-functionalized sheets. In sum, the calculations demonstrated that the carboxyl group plays a crucial role in the anchoring of urea and thiourea molecules in graphene sheets. The changes in HOMO and LUMO changes emerged by the type of anchoring, and nitrogen doping could be reflected in the voltammetry measurements, as shown earlier.

3. Conclusion

We produced carbonaceous materials from GO and graphite. Sulfur and nitrogen were incorporated into the carbonaceous materials by the mechanochemical method. We followed three different routes 1) pristine graphite, and GO subjected to a BM treatment, 2) pristine material (GO or graphite) mixed with

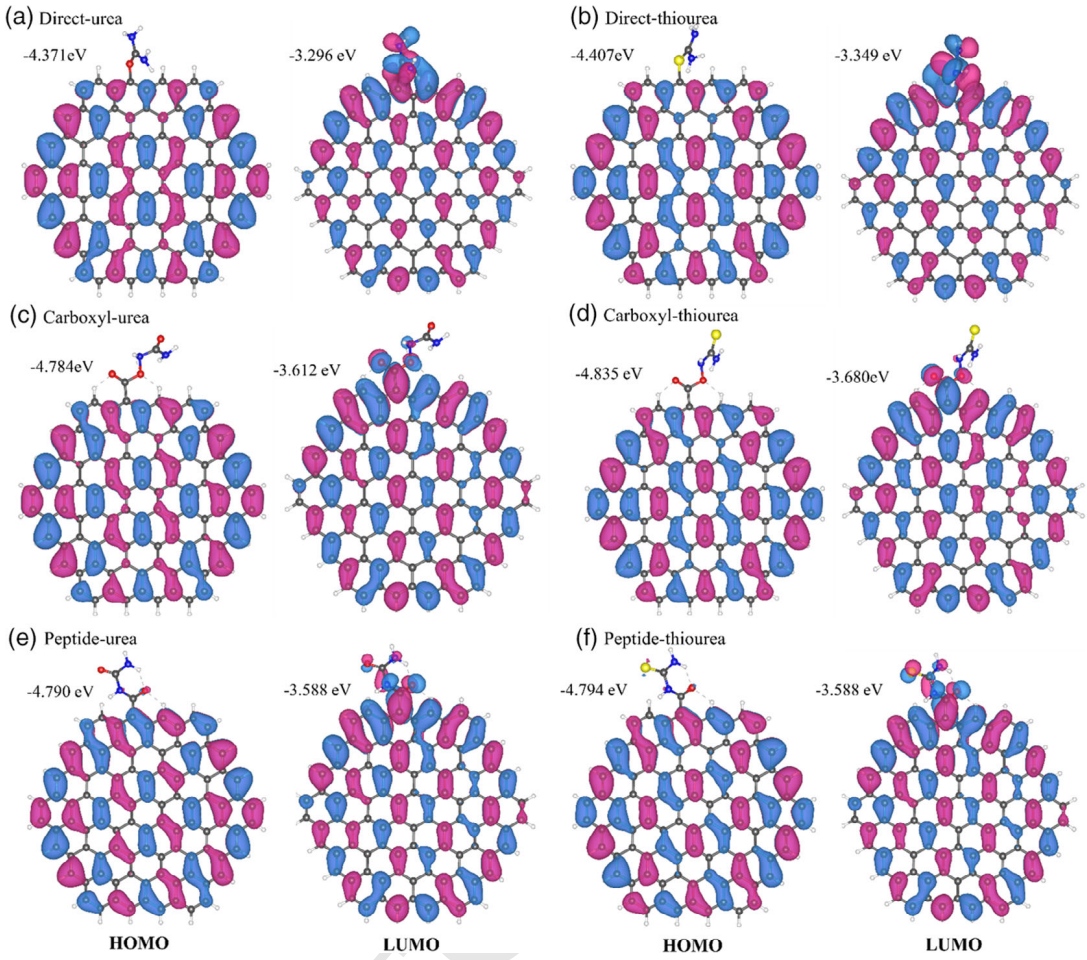

Figure 13. HOMO and LUMO wave functions and the corresponding energies of urea and thiourea molecules covalently attached to the graphene sheet $C_{96}H_{24}$ edges. The wave functions were plotted at the isosurface of ± 0.03 Å$^{-3/2}$. The colors refer to the positive (blue) and negative (purple) phase of the wave function.

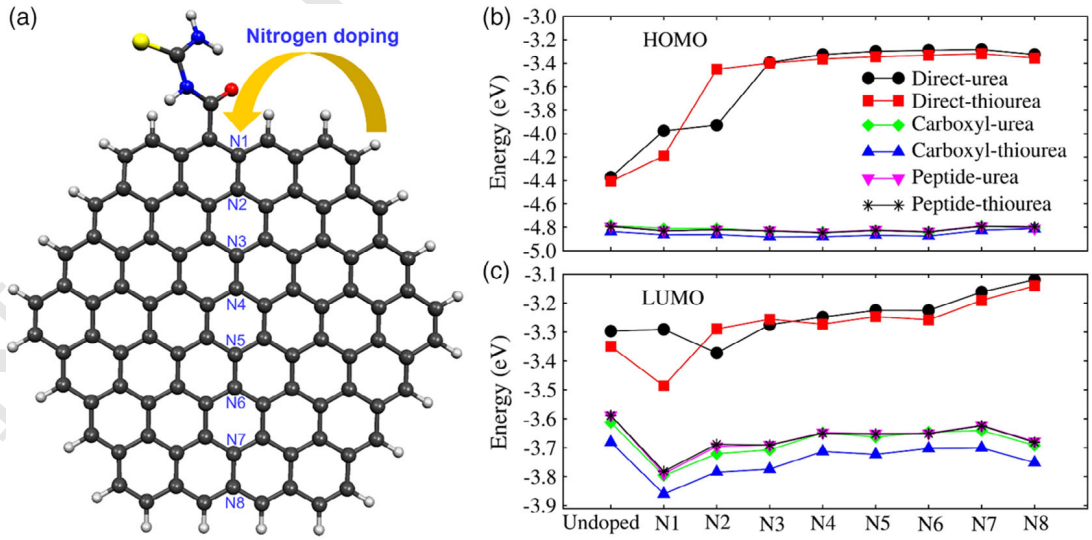

Figure 14. a) Ball-stick model of a particular system (peptide–thiourea) showing how the nitrogen is incorporated in $C_{96}H_{24}$ graphene sheets. Thus, a single carbon atom indicated by N1, N2, N2, N3, N4, N5, N6, N7, and N8 is removed and replaced by nitrogen. b,c) HOMO and LUMO energies for urea and thiourea for the nitrogen-doped cases. The energies corresponding to undoped cases are also shown.

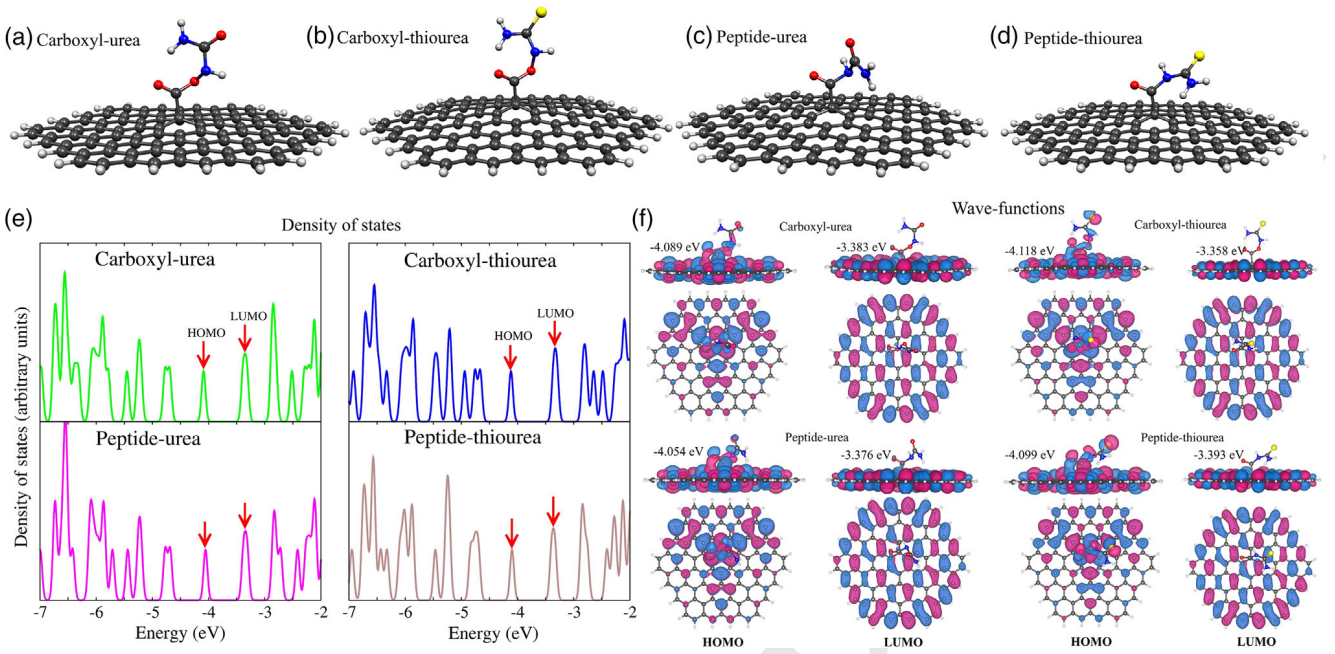

Figure 15. a–d) Ball-stick model of the optimized structures of graphene sheets $C_{96}H_{24}$ with urea and thiourea molecules covalently anchored through the carboxyl group. e) Corresponding density of states and f) HOMO and LUMO wave functions (top and side views). The HOMO and LUMO energies are indicated. The wave functions were plotted at the isosurface of ± 0.03 Å$^{-3/2}$.

thiourea powder and exposed to a BM treatment, 3) pristine material (GO or graphite) mixed with urea and subjected to a BM treatment. After the mechanochemical process reduced the GO samples, the usage of urea and thiourea enhance N, N—S doping. Different functional groups containing C, N, and O, and S were hosted at the milled sample surface when urea and thiourea were introduced into the BM treatment. We have also shown that all carbonaceous materials exhibited oxidation temperature intermediates between the GO and graphite pristine. The specific capacitance performance in milled GO samples was smaller, compared with milled graphite samples.

DFT calculations demonstrated that urea and thiourea were chemisorbed at the graphene sheets' edges and surface through carboxyl groups. Our results also revealed that urea and thiourea were covalently joined only to the edges of the graphene sheet through their oxygen or sulfur and in the absence of carboxyl groups (direct link). The HOMO energies analysis revealed that these direct-link cases and those joined to the surface through carboxyl group cases are energetically more susceptible to oxidation. Further results demonstrated that nitrogen doping in direct-link cases decreases the HOMO energy; thus, the nitrogen could improve these oxidization processes.

For the first time, a simultaneous N, S doping and GO paper-like reduction using a dry HEBM methodology was achieved with a predissolved water-soluble urea/thiourea molecule. Our results showed a low-cost, environmentally-friendly, practical, and scalable mechanochemical method for N/S doping graphitic material that opens a range of possibilities for other heteroatom dopants and water-soluble molecules. The thiourea molecule had a higher reducing chemical activity than urea in the GO dispersions, which exhibited interlayer cross-linking and sulfur linkages with the milling process. Our results demonstrated that the HEBM method was energetically efficient in reducing the GO, analogous to inert atmosphere heat treatment to remove or reduce carboxylic and epoxide groups.

4. Experimental Section

Pristine GO was synthesized by the modified Hummer's method. This purified GO aqueous suspension reached 3.6 mg mL^{-1} fraction of mas and was then degassed (≈ -0.1 MPa) for 30 min to avoid gas bubbles during GO film deposition. Thiourea (CH_4N_2S, Sigma-Aldrich, Prod. #62-56-6, $\geq$99 wt% purity) and urea (CH_4N_2O, Sigma-Aldrich, Prod. #57-13-6, $\geq$99 wt% purity) molecules were used as N, S containing doping source. For GO synthesis and graphite HEBM experiments, we used raw mineral graphite mesh #32 + 99% purity from Asbury-Carbons Company. One GO dissolutions control and two GO doping dissolutions were prepared: all GO dissolutions–GO film, GO + thiourea, and GO + urea (Table S2, Supporting Information), were magnetically stirred at 400 rpm for 15 min, and bath sonicated for 15 min, whereafter the urea and thiourea molecules were dispersed uniformly.

Prior to BM process, paper-like GO films were deposited via drop-casting technique on 15 cm × 15 cm mold release over a tempered glass substrate at 70 °C for 72 h. Thereafter, dried GO films were used to fabricate pills as a freestanding film, with GO films area density of 4.31, 4.35, and 4.71 mg cm^{-2} for GO, GO + thiourea, and GO + urea films, respectively. In a typical experiment, 800 mg of ground material was introduced into a 65 mL stainless ball-grinding jar (8007—stainless-steel grinding vial set) with ten stainless planetary balls mill with diameters 12 mm × 3 pc, 6 mm × 4 pc, 5 mm × 1 pc, 4 mm × 1 pc, and 3 mm × 1 pc. The average ball to powder mass ratio (BPMR) was 36:1 for all grinding experiments. Milling experiments were run in 8000D Mixer/Mill quipment at 1725 rpm speed along 80 min under nongas inert conditions. The BM materials were collected and labeled as GO-BM, GO-T-BM, and GO-U-BM, corresponding to pristine GO, GO mixed with thiourea, and GO mixed with urea dissolutions, respectively

(Figure S1, Supporting Information). On the other hand, the same mechanochemical methodology, contrasting with graphite flakes in dry heterogeneous grinding mixes with the same N, N—S containing source molecules without a post-purification process. Then, we prepared one graphite sample control and two dry heterogeneous mixed samples: graphite, graphite + thiourea, and graphite + urea (Table S1, Supporting Information). After milling, the collected material was labeled as G-BM, G-T-BM, and G-U-BM, corresponding to graphite, graphite mixed with thiourea, and graphite mixed with urea, respectively (Figure S2, Supporting Information).

SEM images and EDX were characterized on an FEI-Helios Nanolab 600. Raman spectra were carried out with a 514 nm laser wavelength in a Raman Renishaw Micro-Raman. TEM and HR-TEM techniques were characterized on FEI Tecnai F30 (300 keV); milled samples were dispersed on ethanol sonication for 10 min, deposited by drop on lacy carbon 300 mesh copper grids and dried. The post-milled powders were made into pills in a hydraulic press CARVER 3925 applying 1500 psi for 10 s fit on 14 mm pellet pressing die set. The extracted pills were weighed and summarized in Table S2, Supporting Information, with an average weight of 80.5 ± 0.6 mg. CV and Linear sweep voltammetry (LSV) techniques were performed in a VSP 300 Potentiostat-Biologic Science Instruments. 4 cm^2 of 904L stainless #80 mesh was used as an Ohmic sample holder with a negligible double-layer signal (Figure S13, Supporting Information). Pill samples (WE) were totally covered by stainless mesh and mechanically fitted by 500 psi uniform area pressure for 5 s. Ag/AgCl electrode was used as a reference electrode (RE), and 2 mm OD × 4 cm Pt wire was used as a counter electrode (CE). Pill samples were CV measured in a three-electrode cell configuration with 0.5 M of H_2SO_4 electrolyte into a window potential range from −0.5 to 1 V versus Ag/AgCl at 10 mV s^{-1} from the open circuit to the cathodic direction. The current–potential (*I*–*V*) curve of GO-film was measured via a two-electrode configuration electrode clamped on the opposite and broadside and using LSV technique within −1 to 1 V potential range at 10 mV s^{-1} speed on GO-film strip of 1 cm × 5 cm. Thermogravimetric analysis (TGA) measurements were carried out using equipment 6000 Perkin Elmer from 50 to 950 °C under the heating rate of 10 °C min^{-1} into a dynamic flow of oxygen (20 mL min^{-1}). Nevertheless, we used dynamic nitrogen flow (20 mL min^{-1}) with the same rate and temperature settings for the GO-film thermogravimetric measurement. X-ray photoelectron spectroscopy (XPS) measurements were carried out on PHI Quantera II (Al Kα). XRD patterns were carried out with a Rigaku Smart Lab (Cu, Kα ≈ 1.54 Å). Attenuated total reflectance–Fourier transform infrared spectroscopy (ATR-FTIR) measurement was performed via Thermo Scientific Nicolet 6700 spectrometer.

Electronic calculations were performed using DFT.[42,43] The generalized gradient approximation with the Perdew, Burke, and Ernzerhof parametrization was chosen for the exchange-correlation functional,[44] as implemented in the SIESTA code.[45] The wave functions for the valence electrons were represented by a linear combination of pseudoatomic numerical orbitals, using a double-ζ polarized basis (DZP),[46] and the core electrons by norm-conserving Troullier–Martins pseudopotentials in the Kleinman–Bylander nonlocal form.[47,48] The real-space grid used for charge and potential integration is equivalent to a plane wave cut-off energy of 150 Ry. Urea (CH_4N_2O) and thiourea (CH_4N_2S) molecules were joined to $C_{96}H_{24}$ graphene sheets and structurally relaxed. Density matrix and energy tolerances were both taken as 10^{-5} eV. Geometry optimization was performed by conjugate gradient minimization until the maximum force was <0.03 eV $Å^{-1}$.

Supporting Information

Supporting Information is available from the Wiley Online Library or from the author.

Acknowledgements

R.S.S. thanks the support from research CONACYT scholarship CVU: 712277. F.L.U. thanks CONACYT for financial support Grant Problemas Nacionales 2016-1-4148. E.M.S. thanks CONACYT for Grant CB-2013-220744. The authors thank LINAN and IPICYT for the characterization facilities, as well as M.Sc. Beatriz A. Rivera-Escoto, Dr. Gladis J. Labrada-Delgado, M.Sc. Ana Iris Peña-Maldonado, and Dr. Héctor G. Silva-Pereyra for technical support. The authors thank Dr. Vicente Rodriguez-González for the facilities for measurements of cyclic voltammetry carried on VSP300 Bio-Logic potentiostat. The authors thank Asbury Carbon Company for graphite mineral donation. The authors thank Shinshu University for the XPS technical support from Obata Michiko and the characterization facilities. The authors thank the National Supercomputing Center (CNS-IPICYT, Thubat Kaal 2.0 HPC configuration). The authors also thank Alberto Hernández-Garcia and Jesus Alanis-Hernández for technical support. The authors thank Prof. David Tománek for their kind advice on using the mechanochemical method in GO reduction.

Conflict of Interest

The authors declare no conflict of interest.

Author Contributions

R.S.S. performed the GO synthesis, conducted milling experiments, and performed TGA, CV, and XRD characterizations. A.M.G. and M.E. contributed to SEM, FTIR, and XRD characterizations. All authors designed the research and wrote the manuscript.

Data Availability Statement

Research data are not shared.

Keywords

ball-milling, doping, graphene oxide, graphite, nitrogen, sulfur

Received: December 2, 2020
Revised: February 10, 2021
Published online:

[1] F. Farjadian, S. Abbaspour, M. A. A. Sadatlu, S. Mirkiani, A. Ghasemi, M. Hoseini-Ghahfarokhi, N. Mozaffari, M. Karimi, M. R. Hamblin, *ChemistrySelect* **2020**, *5*, 10200.
[2] P. P. Brisebois, M. Siaj, *J. Mater. Chem. C* **2020**, *8*, 1517.
[3] L. Zhao, X. L. Guo, L. G. Song, Y. Song, G. Z. Dai, J. P. Liu, *Constr. Build. Matter.* **2020**, *241*, 117939.
[4] M. Daniyal, B. Liu, W. Wang, *Curr. Med. Chem.* **2020**, *27*, 3665.
[5] Q. Zhang, Q. X. Hou, G. X. Huang, Q. Fan, *Environ. Sci. Pollut. Res.* **2020**, *27*, 190.
[6] X. L. Liu, R. Ma, X. X. Wang, Y. Ma, Y. P. Yang, L. Zhuang, S. Zhang, R. Jehan, J. R. Chen, X. K. Wang, *Environ. Pollut.* **2019**, *252*, 62.
[7] M. N. I. Amir, A. Halilu, N. M. Julkapli, A. Ma'amor, *J. Ind. Eng. Chem.* **2020**, *83*, 1.
[8] N. Zhang, W. X. Qi, L. L. Huang, E. Jiang, E. J. Bao, X. Zhang, B. G. An, G. He, *Chin. J. Chem. Eng.* **2019**, *27*, 1348.
[9] S. M. Mousavi, S. A. Hashemi, Y. Ghasemi, A. M. Amani, A. Babapoor, O. Arjmand, *Drug Metab. Rev.* **2019**, *51*, 12.
[10] Y. Wang, S. S. Li, H. Y. Yang, J. Luo, *RSC Adv.* **2020**, *10*, 15328.
[11] Y. Zhang, K. Su, Z. Li, *J. Membr. Sci.* **2018**, *563*, 718.

[12] J. Yang, D. Gong, G. Li, G. Zeng, Q. Wang, Y. Zhang, G. Liu, P. Wu, E. Vovk, Z. Peng, X. Zhou, Y. Yang, Z. Liu, Y. Sun, *Adv. Mater.* **2018**, *30*, 1705775.
[13] Y. Xue, H. Chen, J. Qu, L. Dai. *2D Mater.* **2015**, *2*, 44001.
[14] C. Liu, X. Liu, J. Tan, Q. Wang, H. Wen, C. Zhang, *J. Power Sources* **2017**, *342*, 157.
[15] F. Dong, Z. Zhao, T. Xiong, Z. Ni, W. Zhang, Y. Sun, W. K. Ho, *ACS Appl. Mater. Interfaces* **2013**, *5*, 11392.
[16] F. Dong, L. Wu, Y. Sun, M. Fu, Z. Wu, S. C. Lee, *J. Mater. Chem.* **2011**, *21*, 15171.
[17] G. Zhang, J. Zhang, M. Zhang, X. Wang, *J. Mater. Chem.* **2012**, *22*, 8083.
[18] W. J. Ong, L. L. Tan, Y. H. Ng, S. T. Yong, S. P. Chai, *Chem. Rev.* **2016**, *116*, 7159.
[19] B. Zhu, P. Xia, W. Ho, J. Yu, *Appl. Surf. Sci.* **2015**, *344*, 188.
[20] L. G. Cancado, M. P. Pimenta, B. R. A. Neves, M. S. S. Dantas, A. Jorio, *Phys. Rev. Lett.* **2004**, *93*, 247401.
[21] G. Keskar, R. Rao, J. Luo, J. Hudson, J. Chen, A. M. Rao, *Chem. Phys. Lett.* **2005**, *412*, 269.
[22] A. Armano, *C-J. Carbon Res.* **2019**, *5*, 67.
[23] A. Eckmann, A. Felten, A. Mishchenko, L. Britnell, R. Krupke, K. S. Novoselov, C. Casiraghi, *Nano Lett.* **2012**, *12*, 3925.
[24] L. Q. Li, X. L. Yao, H. L. Li, Z. Liu, W. W. Ma, X. Liang, *J. Chem. Eng. Jpn.* **2014**, *47*, 21.
[25] D. A. Dikin, S. Stankovich, E. J. Zimney, R. D. Piner, G. H. B. Dommett, G. Evmenenko, S. T. Nguyen, R. S. Ruoff, *Nature* **2007**, *448*, 457.
[26] H. J. Park, J. Meyer, S. Roth, V. Skakalova, *Carbon* **2010**, *48*, 1088.
[27] R. Cruz-Silva, A. Morelos-Gomez, H. I. Kim, H. K. Jang, F. Tristan, S. Vega-Diaz, L. P. Rajukumar, A. L. Elias, N. Perea-Lopez, J. Suhr, M. Endo, M. Terrones, *ACS Nano* **2014**, *8*, 5959.
[28] S. Wang, S. Wang, Q. Y. Gao, J. C. Wang, *J. Phys. Chem. B* **2005**, *109*, 17281.
[29] C. B. Dai, H. Y. Zhang, R. D. Li, H. F. Zou, *Pol. J. Chem. Technol.* **2019**, *21*, 35.
[30] N. Rahmanian, S. Naderi, E. Supuk, R. Abbas, A. Hassanpour, *Procedia Eng.* **2015**, *102*, 174.
[31] J. Ederer, P. Janos, P. Ecorchard, J. Tolasz, V. Stengl, H. Benes, M. Perchacz, O. Pop Georgievski, *RSC Adv.* **2017**, *7*, 12464.
[32] C. K. Chua, M. Pumera, *Chem. Eur. J.* **2015**, *21*, 12550.
[33] F. López-Urías, J. L. Fajardo-Díaz, *Phys. Chem. Chem. Phys.* **2020**, *22*, 4533.
[34] F. López-Urías, J. L. Fajardo-Díaz, *Appl. Surf. Sci.* **2020**, *521*, 146435.
[35] F. López-Urías, J. L. Fajardo-Díaz, A. J. Cortés-López, C. L. Rodriguez-Corvera, L. E. Jimenez-Ramírez, E. Muñoz-Sandoval, *Adv. Theory Simul.* **2020**, *3*, 1900219.
[36] J. F. Zhao, K. Chen, B. Yang, Y. N. Zhang, C. X. Zhu, Y. X. Li, Q. C. Zhang, L. H. Xie, W. Huang, *RSC Adv.* **2017**, *7*, 53770.
[37] P. T. Lee, D. Lowinsohn, R. G. Compton, *Electroanalysis* **2014**, *26*, 1488.
[38] S. Witomska, Z. Y. Liu, W. Czepa, A. Aliprandi, D. Pakulski, P. Pawluc, A. Ciesielski, P. Samori, *J. Am. Chem. Soc.* **2019**, *141*, 482.
[39] Z. G. Wang, P. J. Li, Y. F. Chen, J. R. He, W. L. Zhang, O. G. Schmidt, Y. R. Li, *Nanoscale* **2014**, *6*, 7281.
[40] S. F. Wang, X. Li, Y. G. Liu, C. Zhang, X. F. Tan, G. M. Zeng, B. A. Song, L. H. Jiang, *J. Hazard. Mater.* **2018**, *342*, 177.
[41] S. A. Wohlgemuth, R. J. White, M. G. Willinger, M. M. Titirici, M. Antonietti, *Green Chem.* **2012**, *14*, 1515.
[42] P. Hohenberg, W. Kohn, *Phys. Rev.* **1964**, *136*, B864.
[43] W. Kohn, L. J. Sham, *Phys. Rev.* **1965**, *140*, A1133.
[44] J. P. Perdew, A. Ruzsinszky, G. I. Csonka, O. A. Vydrov, G. E. Scuseria, L. A. Constantin, X. Zhou, K. Burke, *Phys. Rev. Lett* **2008**, *100*, 136406.
[45] J. M. Soler, E. Artacho, J. D. Gale, A. García, J. Junquera, P. Ordejón, D. Sánchez-Portal, *J. Phys. Condens. Matter* **2002**, *14*, 2745.
[46] J. Junquera, O. Paz, D. Sánchez-Portal, E. Artacho, *Phys. Rev. B* **2001**, *64*, 235111.
[47] N. Troullier, J. L. Martins, *Phys. Rev. B* **1991**, *43*, 1993.
[48] L. Kleinman, D. M. Bylander, *Phys. Rev. Lett.* **1982**, *48*, 1425.

